

VET: Visual Error Tomography for Point Cloud Completion and High-Quality Neural Rendering

LINUS FRANKE, Friedrich-Alexander-Universität Erlangen-Nürnberg, Germany

DARIUS RÜCKERT, Friedrich-Alexander-Universität Erlangen-Nürnberg, Germany and Voxray GmbH, Germany

LAURA FINK, Friedrich-Alexander-Universität Erlangen-Nürnberg, Germany and Fraunhofer IIS, Germany

MATTHIAS INNEMANN, NavVis GmbH, Germany

MARC STAMMINGER, Friedrich-Alexander-Universität Erlangen-Nürnberg, Germany



Fig. 1. The initial point cloud of the CHERRY TREE lacks completeness, with branches and leaves missing. Neural point-based rendering exhibits severe artifacts in these regions (*left*). By applying VET and spawning new points, we can complete the point cloud efficiently. This appearance-driven geometric completion improves quality of the neural rendering significantly (*middle*) thus outperforming state of the art methods (*right*).

In the last few years, deep neural networks opened the doors for big advances in novel view synthesis. Many of these approaches are based on a (coarse) proxy geometry obtained by structure from motion algorithms. Small deficiencies in this proxy can be fixed by neural rendering, but larger holes or missing parts, as they commonly appear for thin structures or for glossy regions, still lead to distracting artifacts and temporal instability. In this paper, we present a novel neural-rendering-based approach to detect and fix such deficiencies. As a proxy, we use a point cloud, which allows us to easily remove outlier geometry and to fill in missing geometry without complicated topological operations. Keys to our approach are (i) a differentiable, blending point-based renderer that can blend out redundant points, as well as (ii) the concept of *Visual Error Tomography* (VET), which allows us to lift 2D error maps to identify 3D-regions lacking geometry and to spawn novel points accordingly. Furthermore, (iii) by adding points as nested environment maps, our approach allows us to generate high-quality renderings of the surroundings in the same pipeline. In our results, we show that our approach can improve the quality of a point cloud obtained by structure from motion and thus increase novel view synthesis quality significantly. In contrast to point growing techniques, the approach can also fix large-scale holes and missing thin structures effectively. Rendering quality outperforms state-of-the-art methods and temporal stability is significantly improved, while rendering is possible at real-time frame rates.

CCS Concepts: • **Computing methodologies** → **Rendering**; **Image-based rendering**; **Reconstruction**.

Additional Key Words and Phrases: Novel View Synthesis, Neural Rendering, Machine Learning, Point Cloud Completion, Computed Tomography

This is the author’s version of the work. It is posted here for your personal use. Not for redistribution. The definitive Version of Record was published in SiggraphAsia’23, <http://dx.doi.org/10.1145/3610548.3618212>

1 INTRODUCTION

Recent advances in neural rendering have shown remarkable results on various tasks. Especially the field of novel view synthesis [Tewari et al. 2022] has received great attention from researchers around the world. Fridovich-Keil et al. [2022] have pointed out that the basis of the success comes from a differentiable rendering pipeline. Thus, researchers have implemented inverse rendering formulations for several scene representations ranging from coordinate networks over volumetric data structures to triangle meshes or point clouds as geometric proxies.

In practice, explicit representations such as triangle meshes or point clouds are often preferred due to their simplicity to use and the possibility to integrate them into existing workflows. Such proxies can be generated using 3D reconstruction techniques on input images or video, or using active 3D scanners. To achieve high render quality, a high-quality proxy is required. However, this is not always available as different capturing modalities fail in different scenarios. Multi-view stereo depth estimation cannot reliably estimate featureless, reflective, or transparent surfaces, and often misses small, fine structures. Active scanners, such as LIDAR, can handle textureless surfaces, but produce artifacts on dark and glossy surfaces and generally exhibit lower resolution. As a result, the proxy geometry often is either incomplete or contains outliers.

In this paper, we propose a method to rectify these issues using a pair of *cleaning* and *spawning* steps. As proxy we use a point cloud, which makes it easy to modify, add, and remove geometry without having to adapt topology. Key to our approach is a differentiable point renderer that considers and optimizes point transparencies.

Points that receive high transparency are considered as outliers and can be removed without impact on quality. This *cleaning* operation enables us to improve the proxy point cloud twofold: first, outliers from the original proxy, as they appear for instance in reflective regions or at object edges, can be removed to clean up the proxy and improve render performance. Second, it opens the door for an effective *spawning* operation: We can tentatively add points in likely undersampled regions and let the cleaning step discard points that do not contribute to better renderings. Thus, the surviving added points improve the proxy with the quality of this point completion being dependent on the accuracy of the prediction for undersampled regions. To identify these critical regions in 3D space, we introduce a method we call Visual Error Tomography (VET). Based on the output of the neural renderer and the corresponding input images, we generate error images and project these back to 3D space using computed tomography. With this step, we can reliably identify 3D regions, where the original 3D reconstruction generated too few points, or no points at all, like at glossy surfaces or thin structures. As we show in our results, this step is much more effective than point growing approaches [Furukawa et al. 2010; Schönberger et al. 2016], which tend to generate many unnecessary points, require many iterations to fill holes, and fail for thin structures. We also show that by spawning (and cleaning) points in a few layers of nested environment maps, it is possible to faithfully re-render the environment, which improves rendering quality considerably.

The teaser image (Fig. 1) shows the point cloud for a tree obtained from multi-view stereo reconstruction along with the corresponding rendering result on the left. In the center, we present the enhanced point cloud, which notably enhances the rendering quality with other methods failing to reconstruct the fine-grain structure of the leafs faithfully. In summary, our key contributions are:

- A fast differentiable neural point-based rasterizer, capable of efficiently handling and optimizing point transparency
- The concept of Visual Error Tomography, a novel technique enabling reliable identification of erroneous 3D regions
- A pipeline incorporating iterative steps of point spawning and cleaning, resulting in the generation of clean and complete proxies, ultimately leading to a significant improvement in rendering quality
- The faithful visual reconstruction of the environment using nested point-based environment maps
- An evaluation of these methods, showing improved render quality particularly in difficult regions
- An open source implementation of the method located at: <https://github.com/lfranke/VET>

2 RELATED WORK

Novel view synthesis (NVS) is the task of generating new views of a scene given a set of input images. For example, one could capture a few photographs of an object and then use NVS to generate a video with an arbitrary camera trajectory. Many NVS implementations make use of image-based rendering techniques by directly warping the colors of several source images to a target view [Chaurasia et al. 2013; Debevec et al. 1998]. However, a geometrically correct warping requires an accurate proxy geometry, which is often not

present on real datasets [Shum and Kang 2000]. Hence, traditional methods produce warping artifacts in rendered images especially around silhouettes. These warping artifacts can be significantly reduced by replacing blending operation in the warping stage with deep neural networks [Hedman et al. 2018; Riegler and Koltun 2020, 2021]. If no proxy geometry is available, learning-based IBR approaches have been developed that create a multi-plane image representation [Mildenhall et al. 2019; Srinivasan et al. 2019; Tucker and Snavely 2020; Zhou et al. 2018] to directly estimate the warp field [Flynn et al. 2016; Ganin et al. 2016; Zhou et al. 2016]. A disadvantage of IBR approaches is that all source images must be present in memory or quickly fetchable to render a novel view.

The desired solution to this problem is to generate a compact 3D representation of the scene in a preprocessing stage using only the source images as an input. After that, novel views can be rendered efficiently without the need of all input images. In the last couple of years, several 3D scene representations have been proposed, all with different advantages and disadvantages [Tewari et al. 2022]. One of the most popular scene representations are coordinate networks, also known as NeRFs [Mildenhall et al. 2021], since they are memory efficient, easy to use, and show excellent results on many datasets. However, evaluating and training NeRF is time-consuming due to the need to evaluate a large neural network for each 3D sample. This has led to a series of subsequent works further improving quality [Barron et al. 2021, 2022, 2023; Martin-Brualla et al. 2021; Yu et al. 2021b; Zhang et al. 2020] or run-time [Müller et al. 2022; Reiser et al. 2021; Turki et al. 2022; Yu et al. 2021a].

Next to coordinate networks, other scene representations such as sparse voxel grids [Fridovich-Keil et al. 2022], octrees [Rückert et al. 2022], tensor factorization [Chen et al. 2022] and triangle meshes [Thies et al. 2019] also show strong results on the NVS task. Another promising scene representation are point clouds, since they can capture arbitrary fine geometric detail and are easy to use and modify. Today it is possible to render billions of points in real time [Schütz et al. 2022] and simultaneously remove typical point-based rendering artifacts using deep neural networks [Meshry et al. 2019; Pittaluga et al. 2019; Song et al. 2020] and learned point descriptors [Aliev et al. 2020; Rakhimov et al. 2022; Rückert et al. 2022].

A key observation to further improve the NVS quality is, that the point cloud and camera parameters used in these approaches can be optimized using differentiable rendering techniques. In the context of point-based graphics, several approaches have been proposed for sphere rendering, Gaussian splatting, and point-sample rendering [Kerbl et al. 2023; Kopanas et al. 2022, 2021; Lassner and Zollhöfer 2021; Wiles et al. 2020; Zhang et al. 2022]. A disadvantage of most of these approaches is that they do not have a reliable way to remove and spawn new points automatically. This hinders rendering quality and leads to artefacts, if the initial point cloud is erroneous. To overcome this problem, Xu et al. [2022] have introduced a point growing strategy to insert new points close to existing ones. Their approach demonstrates improved rendering quality on real datasets. Similarly, Kerbl et al. [2023] split large Gaussians in their pipeline to introduce new points. Their point growing strategies however may not effectively handle regions where few existing points are available for reference, as well as issues with growth criteria selections [Poux

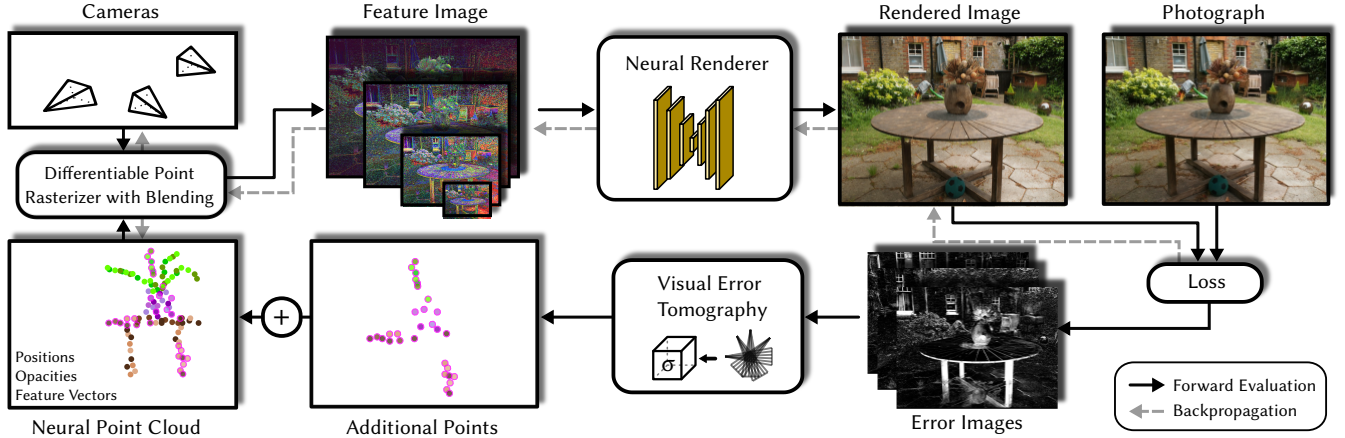


Fig. 2. Overview of our neural rendering pipeline with visual error tomography. Point descriptors, positions and opacities are optimized via backpropagation, which automatically removes outliers during training. After initial convergence, our VET is used to predict missing 3D points from the error images. Following the optimization is resumed until the next convergence. This process is repeated 1-3 times depending on scene complexity.

et al. 2022] can be present. To this end, Zuo and Deng [2022] propose an improved spawning technique, which identifies pixels with large rendering error and spawns new points randomly along the ray passing these pixels. While this approach allows for reconstruction of missing objects, it is worth mentioning that only a limited number of points are placed on the object’s surface. As a consequence, the reconstruction process can require thousands of iterations to complete and is prone to overfitting if points are spawned to close to the cameras.

Core of our method is *visual error tomography* (VET), which is based on *computed tomography* (CT). CT reconstructs 3D volumetric densities from a series of volumetric projections as obtained by x-ray imaging [Buzug 2008]. In our pipeline, we use Neural Adaptive Tomography (NeAT) [Rückert et al. 2022] for CT reconstruction, because this approach can generate sharp, detailed reconstructions, and is able to model a non-linear intensity response of ray integrals, which is required for our non-physical reconstruction task.

3 OVERVIEW

Fig. 2 provides an overview of our pipeline. We start with a set of photographs, their corresponding poses, and an initial point cloud representing the scene. Each point in the cloud is assigned a four-dimensional feature vector and an alpha value denoting opacity. A differentiable point rasterizer renders the point cloud to feature images in multiple resolutions, which are then passed through a neural rendering U-Net to generate the final renderings [Aliev et al. 2020]. The render loss is used to update point features and opacities via backpropagation. Depending on the initial quality of the reconstruction, optimization is performed on point positions and camera poses in this stage [Kopanas et al. 2022; Rückert et al. 2022]. Points with low opacity are identified as outliers and automatically removed during the optimization. Further details regarding the differentiable renderer and the cleaning procedure are provided in Sec. 4. Remaining image errors indicate missing geometry in the proxy. To identify these undersampled regions, we apply our novel

VET and spawn additional points in the found critical regions. In Sec. 5, we provide details about VET and point spawning. The entire process is repeated 1 to 3 times until convergence, dependent on scene complexity. As a result, we obtain a high-quality point cloud of the scene, which can be rendered by a real-time neural rendering system in photo-realistic quality.

4 POINT CLOUD OPTIMIZATION AND CLEANING

As initial point cloud we use the result generated by state-of-the-art 3D reconstruction pipelines such as COLMAP [Schönberger et al. 2016]. In our examples, we use the densified point cloud, but as we show in the evaluation, starting with the sparse point cloud (similar to Kerbl et al. [2023]) and relying on our pipeline to fill in missing points still produces reasonable results.

To better represent the environment, previous methods usually use environment maps [Rückert et al. 2022; Zhang et al. 2020], recently in the form of multi-sphere images [Fridovich-Keil et al. 2022]. In the same spirit, we spawn points on four layers of nested spherical environment maps using spherical Fibonacci sampling [Fink et al. 2019; Keinert et al. 2015] of 0.5M points. These points are optimized and cleaned identically to the original scene points. In particular with the opacity bias for unseen points (Sec. 4.3) this results in sparse and efficient environment maps and high-quality reconstructions of the surrounding.

4.1 Differentiable Point Rasterizer with Blending

Our differentiable point-based rasterization approach is based on the work of Rückert et al. [2022]. For detailed information on the forward and backward pass we refer to the original paper. Our contribution to this pipeline is the use of front-to-back alpha blending instead of the fuzzy depth-test. To that end, we first render the points to per-pixel linked lists, sort these lists by each point’s depth, and finally blend the colors front to back by the respective alpha value.

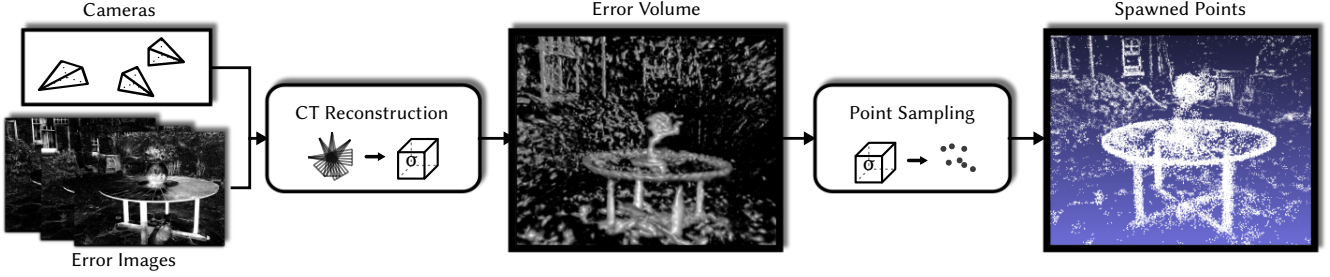


Fig. 3. Visual Error Tomography: starting from error images (left), we apply computed tomography to reconstruct a 3D error volume grid (center). Within each voxels, random points are spawned, where the number of spawned points depends on the voxel’s error value (right).

The final color $C_{u,v}$ with alpha blending is defined as

$$C_{u,v} = \sum_{m=1}^{|\lambda|} T_m \cdot \alpha_m \cdot c_m \quad (1)$$

where λ is the sorted per-pixel linked list, α_m the alpha value, and c_m the respective color of point m . The transmission variable T_m describes how much light passes through all previous points in the list and therefore ensures that points at the end of the list only have a small contribution to the final color: $T_m = \prod_{i=1}^{m-1} (1 - \alpha_i)$. Since Eq. (1) is differentiable, we can integrate this blending approach into the rasterization pipeline of Rückert et al. [2022] to optimize the alpha value of each point. For a better optimization, alpha is stored in the range $(-\infty, \infty)$ and only converted to $[0, 1]$ during blending using the sigmoid function.

The rendering is performed four times with progressively lower resolutions and these are fed into a multi-scalar U-net with gated convolutions followed by a neural camera sensor module, as described by Aliev et al. [2020] and Rückert et al. [2022]. The multi-pixel rendering is implemented efficiently with a custom CUDA per-pixel counting and collection pass [Selgrad et al. 2015] followed by fast GPU bitonic sorting [Batcher 1968; Franke et al. 2018]. For the backwards pass, only the sorted per-pixel lists have to be stored.

4.2 Point Cleaning

The previous optimization adapts the opacity of each point. It is reasonable to assume that outlier points will receive low or zero opacity. We thus determine outliers by introducing a threshold on the alpha value. We found that during optimization, a threshold of 0.3 works well on all tested scenes and gets rid of most outliers, while leaving room for variance during training. For faster training, we remove points below this threshold every 50 epochs.

While previous neural point rendering approaches show some capability for disregarding outliers, mainly through strong masking abilities of gated convolutions, using this explicit optimization of a point confidence proves very powerful in removing outliers, which are either part of the initial reconstruction, environment spheres, or have been added by our spawning step.

4.3 Point Opacity Bias

In our point cloud optimization process, we add $\epsilon = 10^{-7}$ to the opacity gradient of each point. This introduces a small bias to the

opacity and encourages the system to remove all dispensable points, as unused points will be pushed towards a small opacity value. These points are often environment map points, far away outliers or inside structures. This bias proves very powerful in reducing point cloud size without impacting rendering quality.

4.4 Transition to Opaque Point Rendering

Compared to direct one pixel point rendering with depth testing [Schütz et al. 2022], the alpha-based point blending required for outlier removal is slower to evaluate. Therefore, if a real-time exploration of the scene is desired, we can smoothly transition our system from alpha blending to opaque depth testing during the optimization stage. To this end, we adjust the sigmoid function, which encodes the raw alpha values α_{raw} , to become more steep over time:

$$\alpha = \text{sigmoid}((10 + f \cdot t) \cdot \alpha_{\text{raw}}), \quad (2)$$

where f is a user defined parameter and t the current optimization step. After the last iteration, the adjusted sigmoid is almost identical to the step function with each point having a binary opacity. For the final rendering, we then use only the opaque points without alpha blending, achieving high-performance real-time rendering of point clouds with 100 millions of points.

5 POINT SPAWNING VIA VET

The core of our point spawning step is visual error tomography (VET, Sec. 5.1), which allows us to identify incomplete regions of the scene (see Fig. 3), where points then are spawned (Sec. 5.2). We apply spawning multiple times when the neural rendering has converged sufficiently, usually every 200 epochs.

5.1 Visual Error Tomography (VET)

The idea of VET is to compute the per-pixel rendering loss of each input image and process these images with a CT reconstruction module. The CT system creates a volumetric model that captures how much each point in space contributes to the visual error. If the CT output for a given 3D point is small, most of the views must have a small visual error at its projected pixel. If the CT output is large, the visual error at the project pixel coordinates must also be large for multiple views.

Visual errors in neural point rendering often stem from missing points, local minima in descriptor optimization, or strong view dependency. For all three, spawning primitives at that location is a

way to improve results. For the first two cases, additional points fill the incomplete geometry or cause descriptor optimization to take additional training impulses. For strong view dependency, adding points allows the blended descriptors to create a multi-layer surface representation that can approximate view-dependent effects. While tackling this is not the explicit contribution of our pipeline (unlike e.g. Kopanas et al. [2022]), it does not hinder our VET’s purpose.

To compute the error volume, we use the state-of-the-art CT reconstruction approach Neural Adaptive Tomography (NeAT) [Rückert et al. 2022]. The major advantage of NeAT is its ability to model the non-linear intensity response of ray integrals, which is an essential property for our case because visual error maps inherently do not follow Beer-Lambert’s law of photon attenuation. Furthermore, the neural regularizer of NeAT prefers high density regions with sharp edges instead of large smooth areas. This has provided better results for our method and produces sharp and clean error volumes, shown for example in Fig. 3.

For the input images, we smooth the error images I with

$$I'(x, y) = \text{clamp}(I(x, y) * (1 + l) - l, 0, 1) \quad (3)$$

to focus on high-error regions and ignoring small noise. We use $l = 0.3$ for our error images.

We observe that VET works well over the whole scene, including inside-out capturing scheme and backgrounds, but we limit the volume extent to keep memory costs low, as otherwise we would need to increase the output grid size (see next section). For this bounding box we use 95% of the inner points of the initial point cloud, as COLMAP or LIDAR commonly have extreme outliers, which are filtered out with this threshold.

5.2 Error Volume Point Spawning

The output of VET is a 512^3 voxel grid containing estimated error values. After normalizing this grid to the range $[0, 1]$, we spawn $n_{(x,y,z)} = \lfloor e_i(x, y, z) \cdot p_{\max} \rfloor$ new points, where e_i is the normalized error value and p_{\max} the maximum number per voxel. We use $p_{\max} = 10$, which typically leads to 10k - 2000k newly inserted points per VET step, but this is highly dependent on the error volume. The positions of the n added points are randomly distributed in the cell. It is important to note that adding too many or inaccurately placed points is not an issue due to the robust outlier removal strategy described in the previous chapter.

Theoretically, this process converges and progressively fewer points are spawned each time, as less and less visual error is represented in the volume. In practice, we spawn points 1-3 times during training, after which no further improvement can be observed. Usually, our spawning and cleaning steps result in point clouds with a similar amount of points as the initial reconstruction, and thus have no significant impact on memory consumption and render times.

6 EVALUATION

6.1 Datasets

We have tested our approach on multiple scenes from different datasets: The Mip-NeRF 360 dataset [Barron et al. 2022] has dense point clouds of 5M to 10M points and image resolutions of around 2500×1600 (half the original capturing). In the Tanks&Temples

Table 1. Training and render times on the GARDEN and PLAYGROUND scenes. The VET reconstruction takes about 15 minutes and is included in our training time. Inference measured on an RTX4090, training on an A100.

Method	Training	Render (GARDEN)	Render (PLAYGROUND)
InstantNGP (8 spp)	0.25 h	1046 ms	1372 ms
Mip-NeRF 360	36 h	38390 ms	18240 ms
ADOP	8 h	30 ms	15 ms
Ours (Blend)	16 h	33 ms	23 ms
Ours (Opaque)	16 h	29 ms	13 ms

dataset [Knapitsch et al. 2017] images were captured with a high-quality RGB camera in full-HD and point clouds of 5M to 12M points. The Sydney OPERA House scene from Lu et al. [2023] has 2.4M points and an image resolution of 1280×676 . The CHERRY TREE was captured by us with a point cloud of 2M points and images of 1500×1000 . All initial reconstructions were done using the COLMAP multi-view stereo pipeline [Schönberger and Frahm 2016]. Additionally, the Redwood [Choi et al. 2016] dataset is used, which is captured with an RGB-D camera, with small image and point cloud resolutions. For all experiments and methods, unless otherwise noted, 5% of the images (every 20th) were left out of the training and used for evaluation.

6.2 Comparison to Related Work

To evaluate the neural rendering performance of our pipeline we have measured the inference quality on several scenes. We compare against state of the art approaches: Three NeRF-based with InstantNGP [Müller et al. 2022] (with their larger configuration), Mip-NeRF 360 [Barron et al. 2022] and Nerf++ [Zhang et al. 2020], a triangle-based approach in Stable View Synthesis [Riegler and Koltun 2021] and a point-based approach with ADOP [Rückert et al. 2022]. Fig. 4 shows a visual comparison on the Tanks&Temples dataset, with the quantitative evaluation presented in Tab. 2. On all scenes, our method outperforms the compared approaches due to our VET-based point cloud completion. Especially noteworthy is our approach’s ability to reconstruct fine detail as well as overall sharpness. In Fig. 12, we showcase four scenes from the Mip-NeRF 360 dataset, observing the same characteristics. Here however, our PSNR scores tend to be lower than Mip-NeRF 360 as slight errors in calibrations and color shifts by the CNN impact this metric proportionally higher while not impacting perceived visual quality [Zuo and Deng 2022]. Our rendering times however are significantly faster than theirs, as seen in Tab. 1.

Video results can be found at: <https://youtu.be/adH6GyqC4Jk>

6.3 Ablation Studies

6.3.1 Evaluation of the Error Metric used in VET. The VET module takes visual error maps as input to compute the error volume. In Tab. 3, we show rendering quality with different VET error metrics on the tree scene. Overall, using SSIM provides the best results as it guides more points to be spawned in thin locations.

6.3.2 Narrowing Factor. In Sec. 4.4, we have introduced a sigmoid narrowing factor to smoothly transition the alpha renderer to traditional depth testing. Tab. 4 shows the experiment with different values of f , with large values impacting quality, as changes are too abrupt during training. We therefore recommend $f = 0.01$.

Table 2. Results on the Tanks&Temples dataset. See also Fig. 4 for a visual comparison.

Method	TRAIN			PLAYGROUND			M60			LIGHTHOUSE		
	LPIPS ↓	PSNR ↑	SSIM ↑	LPIPS ↓	PSNR ↑	SSIM ↑	LPIPS ↓	PSNR ↑	SSIM ↑	LPIPS ↓	PSNR ↑	SSIM ↑
NeRF++	0.434	18.05	0.579	0.441	22.25	0.613	0.360	23.06	0.728	0.386	20.08	0.662
SVS (half res.)	0.267	17.44	0.683	0.291	22.12	0.704	0.197	23.74	0.831	0.264	17.14	0.722
InstantNGP	0.335	20.46	0.644	0.418	18.69	0.518	0.203	24.97	0.797	0.285	22.98	0.728
Mip-NeRF 360	0.355	18.37	0.624	0.271	24.86	0.736	0.189	24.68	0.838	0.235	21.35	0.750
ADOP	0.131	21.44	0.723	0.126	24.85	0.719	0.103	24.91	0.811	0.119	22.27	0.755
Ours	0.123	21.67	0.765	0.124	25.49	0.768	0.080	27.34	0.875	0.094	24.19	0.808

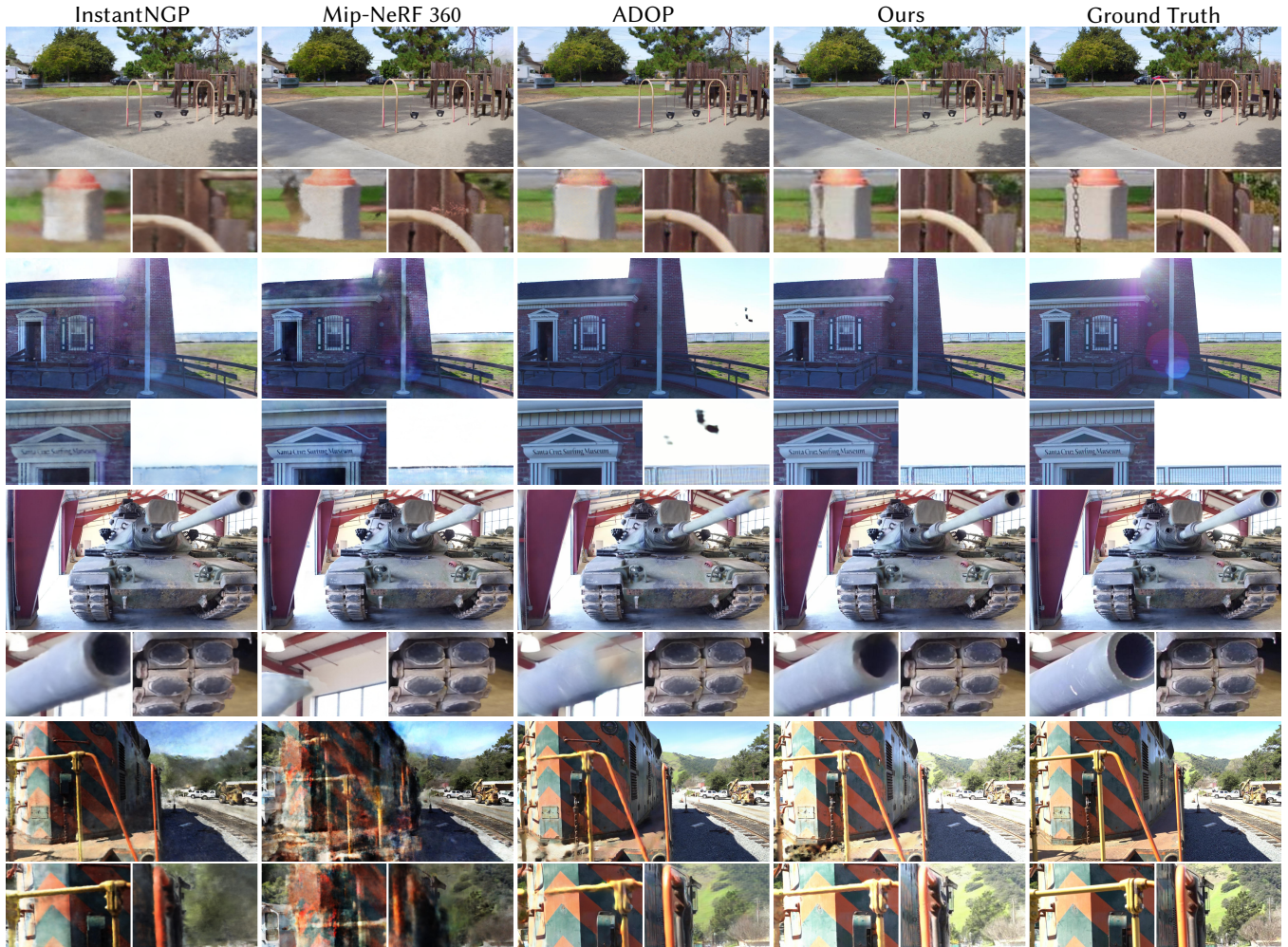


Fig. 4. Comparison to prior work on the Tanks&Temples dataset. Our method is able to reconstruct fine details, remove outliers and improve overall sharpness.

6.3.3 TV Regularization in VET. The neural CT reconstruction approach uses a total variation (TV) regularizer to smooth the output volume. We have tested our pipeline with different TV values and found that with a smaller value, more outlier points are spawned. However, since these points are cleaned reliably, the difference in the final result is only marginal (see Fig. 5). For the remaining experiments we use $tv = 0.001$ as it is a good compromise between capturing small details and not spawning too many outliers.

6.3.4 Point Cleaning. To test the robustness of the outlier cleaning strategy, we have ran our pipeline on the PLAYGROUND scene, where we have added one million additional random points around the playground items. As shown in Fig. 6 (top) on the right, the final point cloud contains almost no visible outliers. On the OPERA scene (Fig. 6 bottom), this robustness provides great cleanup in water areas, where outliers are placed over the water surface through COLMAP’s reconstruction.

Table 3. Rendering error when different visual error metrics are used for the VET reconstruction on the CHERRY TREE scene. L2 error is processed with $l = 0.01$.

VET-loss	LPIPS ↓	PSNR ↑
use L1	0.177	21.57
use L2	0.187	21.19
use SSIM	0.162	21.88

Table 4. Sigmoid narrowing factor f used for transitioning to depth-test based rendering on the Redwood CHAIR scene. After 400 epochs, the switch was initiated, final result after 600 epochs.

f	LPIPS ↓	PSNR ↑
10^0	0.200	18.85
10^{-1}	0.197	18.90
10^{-2}	0.186	19.66
10^{-3}	0.191	19.44

Table 5. Point opacity bias ablation study on the GARDEN scene (7.8M points). Higher bias aggressively removing points while still maintaining low rendering loss.

Bias	Points	LPIPS ↓	PSNR ↑	T	Points	LPIPS ↓	PSNR ↑
10^{-5}	0.2M	0.406	20.73	0.10	10.3M	0.176	23.74
10^{-6}	4.3M	0.186	23.60	0.20	9.1M	0.177	23.69
10^{-7}	7.3M	0.178	23.70	0.30	7.3M	0.178	23.70
10^{-8}	8.0M	0.177	23.71	0.50	6.6M	0.179	23.62
10^{-9}	8.9M	0.178	23.67	0.70	5.3M	0.183	23.67
10^{-10}	9.6M	0.178	23.67	0.90	2.6M	0.200	23.44
				0.99	0.1M	0.446	19.08

Table 6. Point cleaning threshold on the GARDEN scene (7.8M points). Point clouds can be cleaned aggressively before impacting rendered results.

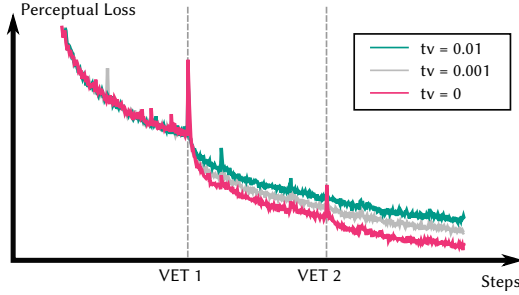


Fig. 5. Loss graph for running VET with different values of the TV regularizer.

Table 7. Amount of points spawned compared with rendering losses.

p_{max}	GARDEN (Init. 7.8M Points)			CHERRY TREE (Init. 2M Points)		
	# Points	LPIPS ↓	PSNR ↑	# Points	LPIPS ↓	PSNR ↑
2	7.0M	0.181	23.60	1.7M	0.295	18.74
5	7.2M	0.180	23.69	1.9M	0.280	19.39
10	7.3M	0.178	23.70	4.0M	0.223	20.41
20	7.8M	0.177	23.71	17.3M	0.182	21.33
30	8.5M	0.177	23.73	31.5M	0.167	21.88

Table 8. Environment map setup on the PLAYGROUND scene (12.5M Points).

Method	# Points	LPIPS ↓	PSNR ↑
No Environment Map	10.0M	0.146	25.34
1 Textured Sphere	11.4M	0.176	24.99
4 Layered Textured Spheres	11.3M	0.181	25.00
1 Point-based Sphere (init. 0.5M points)	10.8M	0.151	24.59
4 P.-b. Layered Spheres (init. 2.0M points)	13.3M	0.124	25.49



Fig. 6. Ablation study on point cleaning. (Top) 1M random points have been added to the PLAYGROUND scene (left) and progressively cleaned (right). On the OPERA scene (bottom), COLMAP has placed points originating from the water incorrectly on land (left), which our pipeline can fix (right).

6.3.5 Point Opacity Bias. In Sec. 4.3, we introduced the opacity bias for the points. As seen in Tab. 5, as long as the bias is not chosen extremely strong, low rendering loss is maintained while the amount of points is efficiently lowered. We choose 10^{-7} for our experiments, however we note that 10^{-6} reduces the point cloud efficiently while still providing sensible, if slightly worse results.

6.3.6 Point Cleaning Confidence Threshold. In every cleaning step, points with confidence below the threshold are removed. As described in Tab. 6, thresholds up to 0.9 still provide reasonable results and reduce point cloud size significantly. However, we use 0.3 for our experiments as it causes point clouds to be similarly sized as the initial COLMAP reconstruction.

6.3.7 Number of Spawned Points per Voxel. As described in Sec. 5.2 we spawn up to p_{max} points per voxel in the error volume. In Tab. 7, the resulting point cloud and the rendering loss is evaluated. We found that $p_{max} = 10$ works well in most cases and keeps total point numbers similar to initial COLMAP reconstructions. Thus we use this for all experiments. We note however that for difficult cases where COLMAP fails considerably, a high p_{max} can improve quality significantly (e.g. in the cherry tree scene, Fig. 1).

6.3.8 Environment Map. As described, we use four layered point-based spheres for our environment map. When compared with different common environment map strategies (see Tab. 8), ours (four point-based spheres) performs best when compared to one point-based sphere or to texture-based environment maps with one [Rückert et al. 2022] or four layers [Yu et al. 2021a]. In contrast to textured maps, our method tends to be less susceptible to overfitting on training view, which in turn improves VET as the error images are more meaningful.

6.4 Point Spawning Accuracy

While our method does not explicitly try to increase geometric accuracy of the input model (but tries to minimize visual loss for novel view synthesis), we evaluate this accuracy on two training scenes of the popular Tanks&Temples benchmark with their F -score based metric [Knapitsch et al. 2017]. As seen in Fig. 7, the point cloud is improved by almost 10% compared to COLMAP if the initial dense reconstruction is not cleaned (*ours-full*), thus only VET-spawned

Method	MEETINGROOM			BARN		
	Prec. \uparrow	Rec. \uparrow	F-score \uparrow	Prec. \uparrow	Rec. \uparrow	F-score \uparrow
COLMAP	0.521	0.247	0.335	0.633	0.553	0.591
Ours	0.507	0.253	0.338	0.631	0.555	0.591
Ours-full	0.512	0.283	0.365	0.624	0.679	0.651

	Initial Point Cloud	Refined Point Cloud	Rendering
	0.335	0.365	
	0.591	0.651	

Fig. 7. Geometric accuracy, measured with the F-score metric [Knapitsch et al. 2017]. Our approach as described (*Ours*) provides similar results in geometry accuracy as COLMAP, while our approach without cleaning the initial point cloud (*Ours-full*) improves scores by about 10%.



Fig. 8. Starting with COLMAP’s sparse reconstruction in our pipeline. Neural rendering without VET (*left*) converges to LPIPS values of 0.596, with VET (*right*) this improves to 0.341.

points are potentially removed. Otherwise, with our normal pipeline, scores are very similar as geometrically accurate points are spawned, but initial correctly placed points might be cleaned if they are not important for visual results of our neural renderer.

6.5 Sparse Colmap Reconstruction as Input

We can also skip COLMAP’s dense reconstruction and directly work with the sparse reconstruction (similar to Gaussian splatting’s pipeline [Kerbl et al. 2023]), thus starting with a point cloud of only 130K points. In this setup, we augment our pipeline with an additional spawning step after 75 epochs, as this low amount of points reaches convergence sooner. As seen in Fig. 8, the resulting point cloud and neural rendering provides overall good results.

Table 9. Comparison with Point-NeRF [Xu et al. 2022] and SNP [Zuo and Deng 2022] on their cropped Tanks&Temples dataset.

Method	BARN (Fig. 9)			Avg. Tanks&Temples		
	LPIPS \downarrow	PSNR \uparrow	SSIM \uparrow	LPIPS \downarrow	PSNR \uparrow	SSIM \uparrow
Point-NeRF	0.120	29.15	0.937	0.080	29.61	0.954
SNP	0.109	29.80	0.915	0.079	29.78	0.942
Ours	0.024	29.66	0.939	0.026	29.54	0.950



Fig. 9. Different point spawning novel synthesis methods. Both Point-NeRF [Xu et al. 2022] and View Synthesis with Sculpted Neural Points (SNP) [Zuo and Deng 2022] use different point spawning strategies with growing and error projection. Both however fail to reconstruct fine details, as with the leaves of the tree.



Fig. 10. Point cloud of the CHERRY TREE enhanced with a point growing strategy (*left*) and our VET (*right*).

6.6 Comparison to Different Spawning Strategies

6.6.1 PointNeRF and SNP. In Fig. 9, we compare to two other novel view synthesis methods using point cloud augmentations on their cropped version of the Tanks&Temples BARN with PointNeRF’s train/eval split. PointNeRF [Xu et al. 2022] spawns points via growing and SNP [Zuo and Deng 2022] samples error map regions continuously in space. Both however fail to reconstruct small details such as the leaves. This is also reflected in the quantitative measurements in Tab. 9, where PSNR and SSIM scores are similar, while we outperform both in LPIPS scores.

6.6.2 Point Growing in our Framework. This result matches with our observations. A point growing strategy implemented in our pipeline instead of VET has the same difficulties while increasing point cloud sizes significantly compared to VET, as seen in Fig. 10. Furthermore unprojecting pixel errors and summing them into voxels (similar to SNP’s strategy) causes point spawns being scattered over larger regions. Solving this either requires thresholding which causes details to be missed or requires to use aggressive point cleaning impacting quality. VET however avoids all these problems.

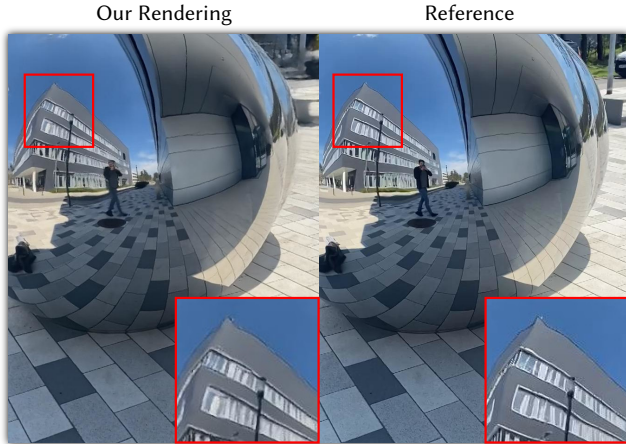


Fig. 11. REFLECTING SPHERES. Our approach can approximate reflections after point cloud cleaning.

6.7 View Dependent Effects

While not explicitly modeled in our approach, our blending renderer can handle view dependencies relatively well (as seen in Fig. 11) by optimizing reflections into multiple point layers. Note however, that very good angular coverage during training is necessary and explicitly modeled approaches such as Kopanas et al. [2022] may be preferable in this use case.

7 LIMITATIONS

We have encountered a few limitations, inherited from the one-pixel point rendering [Aliiev et al. 2020], which is efficient but produces artifacts in rare cases. When the camera gets too close to a surface, the neural rendering network is not able to close the holes between the points and thus the surface behind the wall becomes visible.

Furthermore, we have observed some temporal instabilities when the camera is moved through the scene slowly, which is a side effect of the discrete one-pixel point rendering because points can only discretely move from one pixel to the next.

8 CONCLUSION

To conclude this paper, we have proposed a point-based neural rendering pipeline that is able to render photo-realistic novel views and can simultaneously refine and complete the input point cloud. Point spawning is implemented using our novel VET technique, which uses the visual error maps to identify and populate undersampled regions of the scene. Outlier points are removed automatically by thresholding their opacity value, which is optimized during the training stage. We have shown in several experiments that our pipeline produces high-quality point clouds, and outperforms current state-of-the-art neural rendering approaches in quality. The source code is available at:

<https://github.com/lfranke/VET>

ACKNOWLEDGMENTS

The authors thank the anonymous reviewers for their valuable feedback and Lukas Meyer for the CHERRY TREE scene. Additionally, we thank Stefan Romberg, Michael Gerstmayr and Tim Habigt for the fruitful discussions as well as NavVis GmbH for providing datasets for testing.

Linus Franke was supported by the Bayerische Forschungsförderung (Bavarian Research Foundation) AZ-1422-20. The authors gratefully acknowledge the scientific support and HPC resources provided by the Erlangen National High Performance Computing Center (NHR@FAU) of the Friedrich-Alexander-Universität Erlangen-Nürnberg (FAU) under the NHR project *b162dc*. NHR funding is provided by federal and Bavarian state authorities. NHR@FAU hardware is partially funded by the German Research Foundation (DFG) – 440719683.

REFERENCES

- Kara-Ali Aliiev, Artem Sevastopolsky, Maria Kolos, Dmitry Ulyanov, and Victor Lempitsky. 2020. Neural point-based graphics. In *European Conference on Computer Vision*. Springer, 696–712.
- Jonathan T. Barron, Ben Mildenhall, Matthew Tancik, Peter Hedman, Ricardo Martin-Brualla, and Pratul P. Srinivasan. 2021. Mip-NeRF: A Multiscale Representation for Anti-Aliasing Neural Radiance Fields. In *Proceedings of the IEEE/CVF International Conference on Computer Vision (ICCV)*. 5855–5864.
- Jonathan T Barron, Ben Mildenhall, Dor Verbin, Pratul P Srinivasan, and Peter Hedman. 2022. Mip-nerf 360: Unbounded anti-aliased neural radiance fields. In *Proceedings of the IEEE/CVF Conference on Computer Vision and Pattern Recognition*. 5470–5479.
- Jonathan T Barron, Ben Mildenhall, Dor Verbin, Pratul P Srinivasan, and Peter Hedman. 2023. Zip-NeRF: Anti-Aliased Grid-Based Neural Radiance Fields. *arXiv preprint arXiv:2304.06706* (2023).
- Kenneth E Batchner. 1968. Sorting networks and their applications. In *Proceedings of the April 30–May 2, 1968, spring joint computer conference*. 307–314.
- T.M. Buzug. 2008. *Computed Tomography: From Photon Statistics to Modern Cone-Beam CT*. Springer. <https://books.google.de/books?id=HBFvngEACAAJ>
- Gaurav Chaurasia, Sylvain Duchene, Olga Sorkine-Hornung, and George Drettakis. 2013. Depth synthesis and local warps for plausible image-based navigation. *ACM Transactions on Graphics (TOG)* 32, 3 (2013), 1–12.
- Anpei Chen, Zexiang Xu, Andreas Geiger, Jingyi Yu, and Hao Su. 2022. TensorRF: Tensorial Radiance Fields. In *Computer Vision – ECCV 2022*, Shai Avidan, Gabriel Brostow, Moustapha Cissé, Giovanni Maria Farinella, and Tal Hassner (Eds.). Springer Nature Switzerland, Cham, 333–350.
- Sungjoon Choi, Qian-Yi Zhou, Stephen Miller, and Vladlen Koltun. 2016. A Large Dataset of Object Scans. *arXiv:1602.02481* (2016).
- Paul Debevec, Yizhou Yu, and George Boshokov. 1998. Efficient view-dependent IBR with projective texture-mapping. In *EG Rendering Workshop*, Vol. 4.
- Laura Fink, Sing Chun Lee, Jie Ying Wu, Xingtong Liu, Tianyu Song, Yordanka Velikova, Marc Stamminger, Nassir Navab, and Mathias Unberath. 2019. Lumipath—towards real-time physically-based rendering on embedded devices. In *Medical Image Computing and Computer Assisted Intervention—MICCAI 2019: 22nd International Conference, Shenzhen, China, October 13–17, 2019, Proceedings, Part V 22*. Springer, 673–681.
- John Flynn, Ivan Neulander, James Philbin, and Noah Snavely. 2016. DeepStereo: Learning to Predict New Views from the World’s Imagery. In *Proceedings of the IEEE conference on computer vision and pattern recognition*. 5515–5524.
- Linus Franke, Nikolai Hofmann, Marc Stamminger, and Kai Selgrad. 2018. Multi-layer depth of field rendering with tiled splatting. *Proceedings of the ACM on Computer Graphics and Interactive Techniques* 1, 1 (2018), 1–17.
- Sara Fridovich-Keil, Alex Yu, Matthew Tancik, Qinhong Chen, Benjamin Recht, and Angjoo Kanazawa. 2022. Plenoxels: Radiance Fields without Neural Networks. In *2022 IEEE/CVF Conference on Computer Vision and Pattern Recognition (CVPR)*. 5491–5500. <https://doi.org/10.1109/CVPR52688.2022.00542>
- Yasutaka Furukawa, Brian Curless, Steven M Seitz, and Richard Szeliski. 2010. Towards internet-scale multi-view stereo. In *2010 IEEE computer society conference on computer vision and pattern recognition*. IEEE, 1434–1441.
- Yaroslav Ganin, Daniil Kononenko, Diana Sungatullina, and Victor Lempitsky. 2016. DeepWarp: Photorealistic Image Resynthesis for Gaze Manipulation. In *European conference on computer vision*. Springer, 311–326.
- Peter Hedman, Julien Philip, True Price, Jan-Michael Frahm, George Drettakis, and Gabriel Brostow. 2018. Deep blending for free-viewpoint image-based rendering. *ACM Transactions on Graphics (TOG)* 37, 6 (2018), 1–15.

- Benjamin Keinert, Matthias Innmann, Michael Sanger, and Marc Stamminger. 2015. Spherical fibonacci mapping. *ACM Transactions on Graphics (TOG)* 34, 6 (2015), 1–7.
- Bernhard Kerbl, Georgios Kopanas, Thomas Leimkuhler, and George Drettakis. 2023. 3D Gaussian Splatting for Real-Time Radiance Field Rendering. *ACM Transactions on Graphics* 42, 4 (2023).
- Arno Knapitsch, Jaesik Park, Qian-Yi Zhou, and Vladlen Koltun. 2017. Tanks and Temples: Benchmarking Large-Scale Scene Reconstruction. *ACM Transactions on Graphics* 36, 4 (2017).
- Georgios Kopanas, Thomas Leimkuhler, Gilles Rainer, Clement Jambon, and George Drettakis. 2022. Neural point catacaustics for novel-view synthesis of reflections. *ACM Transactions on Graphics (TOG)* 41, 6 (2022), 1–15.
- Georgios Kopanas, Julien Philip, Thomas Leimkuhler, and George Drettakis. 2021. Point-Based Neural Rendering with Per-View Optimization. *Computer Graphics Forum (Proceedings of the Eurographics Symposium on Rendering)* 40, 4 (June 2021). <http://www-sop.inria.fr/revs/Basilic/2021/KPLD21>
- Christoph Lassner and Michael Zollhofer. 2021. Pulsar: Efficient Sphere-Based Neural Rendering. In *Proceedings of the IEEE/CVF Conference on Computer Vision and Pattern Recognition (CVPR)*. 1440–1449.
- Chongshan Lu, Fukun Yin, Xin Chen, Tao Chen, Gang Yu, and Jiayuan Fan. 2023. A Large-Scale Outdoor Multi-modal Dataset and Benchmark for Novel View Synthesis and Implicit Scene Reconstruction. *arXiv preprint arXiv:2301.06782* (2023).
- Ricardo Martin-Brualla, Noha Radwan, Mehdi SM Sajjadi, Jonathan T Barron, Alexey Dosovitskiy, and Daniel Duckworth. 2021. NeRF in the Wild: Neural Radiance Fields for Unconstrained Photo Collections. In *Proceedings of the IEEE/CVF Conference on Computer Vision and Pattern Recognition*. 7210–7219.
- Moustafa Meshry, Dan B Goldman, Sameh Khamis, Hugues Hoppe, Rohit Pandey, Noah Snavely, and Ricardo Martin-Brualla. 2019. Neural rerendering in the wild. In *Proceedings of the IEEE/CVF Conference on Computer Vision and Pattern Recognition*. 6878–6887.
- Ben Mildenhall, Pratul P Srinivasan, Rodrigo Ortiz-Cayon, Nima Khademi Kalantari, Ravi Ramamoorthi, Ren Ng, and Abhishek Kar. 2019. Local Light Field Fusion: Practical View Synthesis With Prescriptive Sampling Guidelines. *ACM Transactions on Graphics (TOG)* 38, 4 (2019), 1–14.
- Ben Mildenhall, Pratul P Srinivasan, Matthew Tancik, Jonathan T Barron, Ravi Ramamoorthi, and Ren Ng. 2021. Nerf: Representing scenes as neural radiance fields for view synthesis. *Commun. ACM* 65, 1 (2021), 99–106.
- Thomas Muller, Alex Evans, Christoph Schied, and Alexander Keller. 2022. Instant neural graphics primitives with a multiresolution hash encoding. *arXiv preprint arXiv:2201.05989* (2022).
- Francesco Pittaluga, Sanjeev J. Koppal, Sing Bing Kang, and Sudipta N. Sinha. 2019. Revealing Scenes by Inverting Structure From Motion Reconstructions. In *Proceedings of the IEEE/CVF Conference on Computer Vision and Pattern Recognition (CVPR)*.
- Florent Poux, C Mattes, Z Selman, and L Kobbelt. 2022. Automatic region-growing system for the segmentation of large point clouds. *Automation in Construction* 138 (2022), 104250.
- Ruslan Rakhimov, Andrei-Timotei Ardelean, Victor Lempitsky, and Evgeny Burnaev. 2022. NPBG++: Accelerating Neural Point-Based Graphics. In *Proceedings of the IEEE/CVF Conference on Computer Vision and Pattern Recognition*. 15969–15979.
- Christian Reiser, Songyou Peng, Yiyi Liao, and Andreas Geiger. 2021. Kilonerf: Speeding up neural radiance fields with thousands of tiny mlps. In *Proceedings of the IEEE/CVF International Conference on Computer Vision*. 14335–14345.
- Gernot Riegler and Vladlen Koltun. 2020. Free View Synthesis. In *European Conference on Computer Vision*. Springer, 623–640.
- Gernot Riegler and Vladlen Koltun. 2021. Stable view synthesis. In *Proceedings of the IEEE/CVF Conference on Computer Vision and Pattern Recognition*. 12216–12225.
- Darius Ruckert, Linus Franke, and Marc Stamminger. 2022. Adop: Approximate differentiable one-pixel point rendering. *ACM Transactions on Graphics (TOG)* 41, 4 (2022), 1–14.
- Darius Ruckert, Yuanhao Wang, Rui Li, Ramzi Idoughi, and Wolfgang Heidrich. 2022. NeAT: Neural Adaptive Tomography. *ACM Trans. Graph.* 41, 4, Article 55 (jul 2022), 13 pages. <https://doi.org/10.1145/3528223.3530121>
- Johannes L Schonberger and Jan-Michael Frahm. 2016. Structure-from-motion revisited. In *Proceedings of the IEEE conference on computer vision and pattern recognition*. 4104–4113.
- Johannes Lutz Schonberger, Enliang Zheng, Marc Pollefeys, and Jan-Michael Frahm. 2016. Pixelwise View Selection for Unstructured Multi-View Stereo. In *European Conference on Computer Vision (ECCV)*.
- Markus Schutz, Bernhard Kerbl, and Michael Wimmer. 2022. Software Rasterization of 2 Billion Points in Real Time. *arXiv preprint arXiv:2204.01287* (2022).
- Kai Selgrad, Carsten Dachsbacher, Quirin Meyer, and Marc Stamminger. 2015. Filtering multi-layer shadow maps for accurate soft shadows. In *Computer Graphics Forum*, Vol. 34. Wiley Online Library, 205–215.
- Harry Shum and Sing Bing Kang. 2000. Review of image-based rendering techniques. In *Visual Communications and Image Processing 2000*, Vol. 4067. SPIE, 2–13.
- Zhenbo Song, Wayne Chen, Dylan Campbell, and Hongdong Li. 2020. Deep Novel View Synthesis from Colored 3D Point Clouds. In *European Conference on Computer Vision*. Springer, 1–17.
- Pratul P Srinivasan, Richard Tucker, Jonathan T Barron, Ravi Ramamoorthi, Ren Ng, and Noah Snavely. 2019. Pushing the Boundaries of View Extrapolation With Multiplane Images. In *Proceedings of the IEEE/CVF Conference on Computer Vision and Pattern Recognition*. 175–184.
- Ayush Tewari, Justus Thies, Ben Mildenhall, Pratul Srinivasan, Edgar Tretschk, W Yifan, Christoph Lassner, Vincent Sitzmann, Ricardo Martin-Brualla, Stephen Lombardi, et al. 2022. Advances in neural rendering. In *Computer Graphics Forum*, Vol. 41. Wiley Online Library, 703–735.
- Justus Thies, Michael Zollhofer, and Matthias Nießner. 2019. Deferred Neural Rendering: Image Synthesis using Neural Textures. *ACM Transactions on Graphics (TOG)* 38, 4 (2019), 1–12.
- Richard Tucker and Noah Snavely. 2020. Single-View View Synthesis With Multiplane Images. In *Proceedings of the IEEE/CVF Conference on Computer Vision and Pattern Recognition*. 551–560.
- Haithem Turki, Deva Ramanan, and Mahadev Satyanarayanan. 2022. Mega-NeRF: Scalable Construction of Large-Scale NeRFs for Virtual Fly-Throughs. In *Proceedings of the IEEE/CVF Conference on Computer Vision and Pattern Recognition*. 12922–12931.
- Olivia Wiles, Georgia Gkioxari, Richard Szeliski, and Justin Johnson. 2020. SynSin: End-to-end View Synthesis from a Single Image. In *Proceedings of the IEEE/CVF Conference on Computer Vision and Pattern Recognition*. 7467–7477.
- Qiangeng Xu, Zexiang Xu, Julien Philip, Sai Bi, Zhixin Shu, Kalyan Sunkavalli, and Ulrich Neumann. 2022. Point-nerf: Point-based neural radiance fields. In *Proceedings of the IEEE/CVF Conference on Computer Vision and Pattern Recognition*. 5438–5448.
- Alex Yu, Ruilong Li, Matthew Tancik, Hao Li, Ren Ng, and Angjoo Kanazawa. 2021a. Plenotrees for real-time rendering of neural radiance fields. In *Proceedings of the IEEE/CVF International Conference on Computer Vision*. 5752–5761.
- Alex Yu, Vickie Ye, Matthew Tancik, and Angjoo Kanazawa. 2021b. pixelnerf: Neural radiance fields from one or few images. In *Proceedings of the IEEE/CVF Conference on Computer Vision and Pattern Recognition*. 4578–4587.
- Kai Zhang, Gernot Riegler, Noah Snavely, and Vladlen Koltun. 2020. Nerf++: Analyzing and improving neural radiance fields. *arXiv preprint arXiv:2010.07492* (2020).
- Qiang Zhang, Seung-Hwan Baek, Szymon Rusinkiewicz, and Felix Heide. 2022. Differentiable point-based radiance fields for efficient view synthesis. *arXiv preprint arXiv:2205.14330* (2022).
- Tinghui Zhou, Richard Tucker, John Flynn, Graham Fyffe, and Noah Snavely. 2018. Stereo Magnification: Learning View Synthesis Using Multiplane Images. *ACM Transactions on Graphics (TOG)* 37, 4 (2018), 1–12.
- Tinghui Zhou, Shubham Tulsiani, Weilun Sun, Jitendra Malik, and Alexei A Efros. 2016. View Synthesis by Appearance Flow. In *European conference on computer vision*. Springer, 286–301.
- Yiming Zuo and Jia Deng. 2022. View Synthesis with Sculpted Neural Points. *arXiv preprint arXiv:2205.05869* (2022).

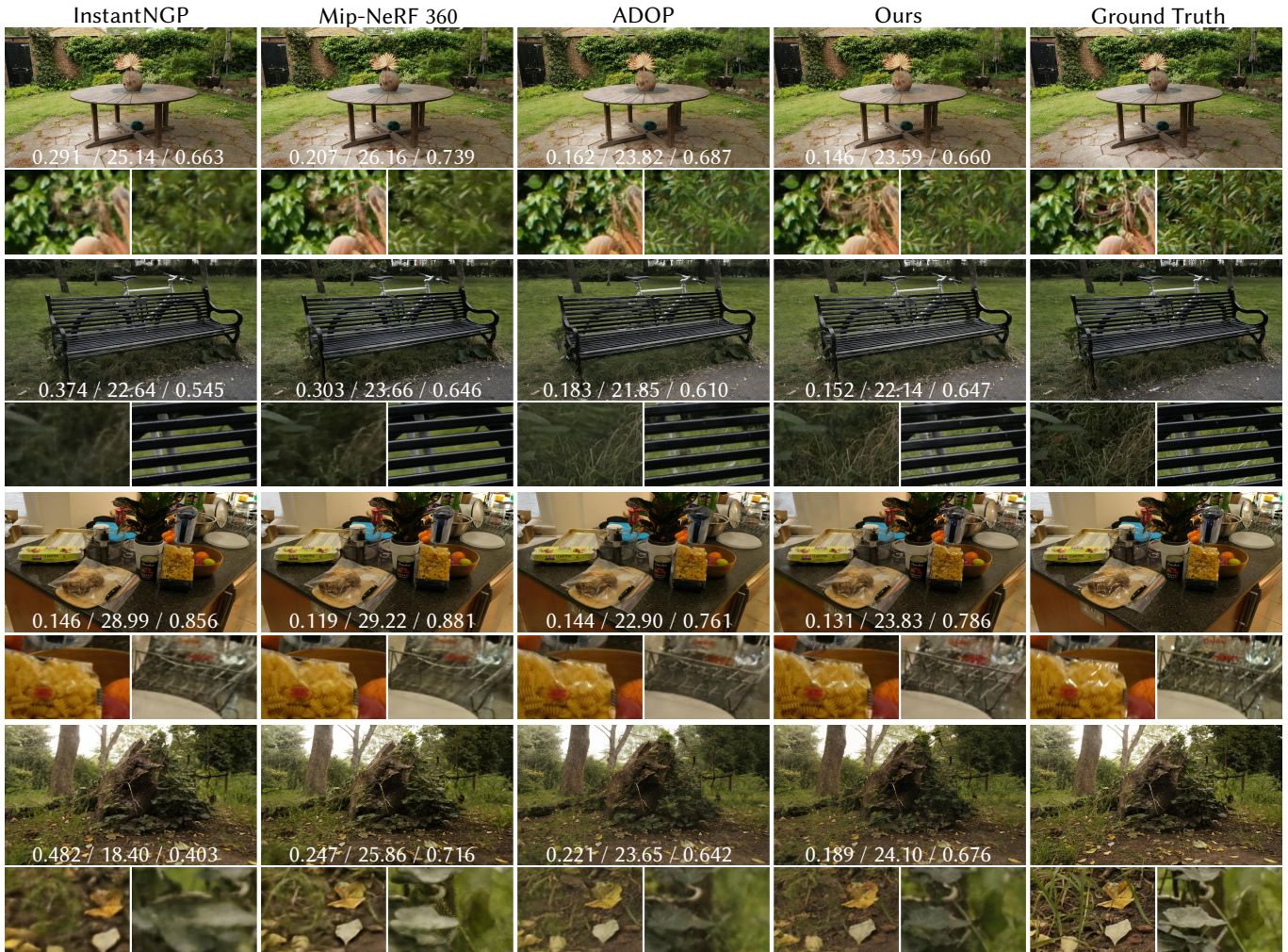


Fig. 12. Comparison on the MipNeRF-360 scenes with the average LPIPS ↓ / PSNR↑ / SSIM↑ scores denoted.